JVST A
Journal of Vacuum Science & Technology A

ARTICLE

pubs.aip.org/avs/jva

Structure and corrosion resistance of electron-beam-strengthened and micro-arc oxidized coatings on magnesium alloy AZ31

Cite as: J. Vac. Sci. Technol. A 41, 053101 (2023); doi: 10.1116/6.0002687
Submitted: 17 March 2023 · Accepted: 5 June 2023 ·
Published Online: 10 July 2023

Yinghe Ma,[1,2,3] Jinhui Mei,[1,2] Junxin Ouyang,[1,2] Peng Wu,[1,2] Sai Wang,[1,2] Jianguo Yang,[1,2,a)] Yanming He,[1,2] Wenjian Zheng,[1,2] Huaxin Li,[1,2] Chuanyang Lu,[1,2] Sendong Ren,[1,2] Jianping Xu,[4] and Paul K. Chu[3,a)]

AFFILIATIONS

[1]Institute of Process Equipment and Control Engineering, Zhejiang University of Technology, Hangzhou 310014, China
[2]College of Mechanical Engineering, Zhejiang University of Technology, Hangzhou 310014, China
[3]Department of Physics, Department of Materials Science and Engineering, and Department of Biomedical Engineering, City University of Hong Kong, Tat Chee Avenue, Kowloon, Hong Kong 150006, China
[4]Department of Materials and Chemical Engineering, Heilongjiang Institute of Technology, Harbin 150050, China

Note: This paper is a part of the 2023 Special Topic Collection on Functional Coatings.
[a)]**Authors to whom correspondence should be addressed:** jgyang@zjut.edu.cn and paul.chu@cityu.edu.hk

ABSTRACT

Micro-arc oxidation (MAO) is very effective to enhance the corrosion performance of Mg alloys. However, the micro-pores in MAO coatings provide a channel for the corrosion medium to reach the alloy matrix. In this work, electron beam strengthening (EBS) is performed to improve the microstructure of the Mg alloy and the MAO coating is prepared subsequently to improve the corrosion performance. The crystalline size of the Mg alloy decreases, the roughness improves, and the corrosion resistance increases. Furthermore, refinement of the grain size by EBS improves the discharge in MAO. The noticeable effect of EBS on the microstructure of the coating lies in the improvement of density, such as porosity reduction by 47.8%. The compactness of the coatings also increases significantly, subsequently improving the corrosion resistance. The corrosion mechanism is proposed.

I. INTRODUCTION

Because of their light weight, high aspect strength, high electromagnetic shielding, and excellent biocompatibility, magnesium alloys have attracted enormous attention in the automobile, electronics, biomedical, and aerospace industries.[1–3] However, the high susceptibility of Mg alloys to corrosion (standard electrode potential of −2.37 V)[4] limits their applications. Micro-arc oxidation (MAO) is very effective to enhance the corrosion performance of magnesium alloys by forming a thick ceramic-like coating with strong adhesion.[5,6] However, micro-pores and micro-cracks frequently exist in MAO coatings like other composite materials,[7–9] consequently increasing the chance of the corrosive medium to reach the substrate to cause fast corrosion.[10–12]

Post-treatment is an effective method for further improving corrosion resistance.[13–17] For example, a significant improvement in the corrosion resistance of the Mg alloy was obtained through the formation of flower-like bis (8-hydroxyquinoline) magnesium inside the micro-pores of MAO coating[14] or the coral reefs-like structure fabricated on the surface of a defective layer.[15] A hybrid organic-inorganic functionalized coating with unique flowery-flake structures deposited on the defective surface of plasma electrolysis (PE) coating via a layer-by-layer self-assembly process of 1-azanaphthalene-8-ol molecules exhibits high corrosion stability.[16] Inorganic-organic layer with outstanding corrosion resistance in a 3.5 wt. % NaCl solution was fabricated by taking advantage of the unique interactions between coumarin (COM) molecules and the

porous layer formed on the Mg alloy.[17] Pretreatment of the substrate prior to MAO is also a viable approach to enhance the mechanical and anticorrosion performance of Mg alloys.[18–20] Specifically, high-energy electron beam bombardment could improve grain homogenization, size, and second phase's distribution to improve the near-surface properties.[21,22] The laser surface melting (LSM) treatment improves the corrosion performance of Mg alloys[23,24] and the dual LSM and MAO techniques have been applied to Mg alloys.[25] The corrosion performance of the coating deposited on the alloy treated by LSM is better than that of the untreated one. The power of an electron beam can be ten times greater than that of a laser beam and metals can more easily absorb electrons. As a result, the energy conversion efficiency can reach 90% that is about ten times that of a laser. However, the research on the use of high-energy electrons to modify the structure and enhance the corrosion performance of Mg alloys is not extensive enough.[26–28] The aim of this work is to systematically elaborate the effects of electron beam strengthening (EBS) on the microstructure and corrosion performance of MAO-coated Mg alloys. The properties of EBS-MAO coatings and MAO coatings prepared at different discharge voltages are studied and compared.

II. EXPERIMENT

A. Electron beam strengthening

The AZ31 Mg alloy ($30 \times 30 \times 2$ mm) was sanded (from 400 to 2000-grit), polished, cleaned ultrasonically in acetone, alcohol, and de-ionized water, and dried in nitrogen before EBS was carried out in an electron beam system (THDW-4) at a pressure below 2×10^{-1} Pa. Table I lists the important instrumental parameters. The EBS specimens were ground, polished, and cleaned ultrasonically prior to MAO. The specimens were labeled EBS-treated or M.P.-treated (M.P.-mechanically ground and polished).

B. Preparation of MAO coatings

A pulsed bi-polar power supply was employed to perform MAO in an electrolyte consisting of 8 g/l Na_2SiO_3, 1 g/l KOH, and 0.5 g/l NaF in distilled water. The anode and the cathode were the Mg alloy and stainless-steel plate, respectively. The main MAO instrumental parameters were positive voltage 460–520 V, negative voltage −40 V, frequency 100 Hz, processing time 20 min, and duty cycle 20%. The coolant system kept the electrolyte temperature below 40 °C. After MAO, the specimens were cleaned thoroughly in distilled water and dried in flowing N_2. The MAO samples with and without EBS at different positive voltages were designated as EBS-MAO-460, EBS-MAO-480, EBS-MAO-500, EBS-MAO-520 and MAO-460, MAO-480, MAO-500, MAO-520, respectively.

TABLE I. Important instrument parameters in the EBS process.

Parameters	
Beam diameter Ø	2 mm
Overlapped track rate	50%
Accelerating voltage U	65 kV
Beam current I_B	0.5 mA
Beam speed v	20 mm/min
Energy input Q	9.75 J/mm

C. Microstructure

Field-emission scanning electron microscopy (SEM, FEI Quanta 200F) was used to examine the morphology and energy-dispersive x-ray spectrometry (EDS) was performed to analyze the elemental composition. A confocal laser microscope (OLYMPUS, OLS5000) was used to screen the surface roughness of EBS and x-ray diffraction (XRD) using a Cu target (0.154 nm) was conducted in the 2θ range between 20° and 80°. An OLYMPUS imager microscope was used to analyze the M.P.-treated and EBS-treated samples. The size, proportion of micro-pores, and porosity of the MAO coatings were analyzed based on the images by IMAGEJ software.

D. Corrosion properties

Potentiodynamic measurements and electrochemical impedance spectroscopy (EIS) were applied to study the corrosion performance of Mg alloys in aqueous 3.5 wt. % NaCl at room temperature. The exposed area of the sample is 1 cm^2. The potentiodynamic polarization tests were conducted from −3.5 to +0.50 V [versus open-circuit potential (OCP)] at a scan rate of 1 mV/s. The positive corrosion potential (E_{corr}) and corrosion current density (i_{corr}) were determined from the Tafel curves and the EIS plots were obtained after immersion for a certain time at an open-circuit potential with an amplitude of 10 mV, and frequency between 100 kHz and 0.1 Hz of AC. The equivalent circuit model (ECM) was used for fitting the electrochemical impedance data of the coated samples. The immersion tests were preceded by exposing the working face of 1 cm^2 (the other faces were sealed before) to a 3.5 wt. % sodium chloride solution at room temperature and photographs were taken at different time points during immersion. After every test, the samples were washed softly with controlled water flow to remove NaCl adhesion, dried with nitrogen, and examined by SEM. The OCP was measured for a period of 5 h in order to establish a stable test.

III. RESULTS AND DISCUSSION

A. Microstructure and chemical composition of the EBS-modified layer

The microstructure of the M. P.-treated sample is given in Fig. 1(a). The Mg alloy consists of polyhedral α-Mg grains. Figures 1(b) and 1(c) depict the surface and polished cross-sectional morphologies near the interface of the modified layer of the EBS-treated sample. EBS produces smaller grains (1/5–1/4 of the original) and a uniform and dense modified layer with a thickness of about 400–500 μm [Fig. 1(d)]. The temperature gradient and solidification rate during the electron beam treatment are very large, consequently producing grain refinement and a smooth interface, which are different from those processed by laser surface melting.[25] Confocal laser microscopy shows that the roughness, Ra, of M.P.-treated is 2.785 μm and that of EBS-treated is 2.155 μm, indicating that EBS decreases the surface roughness.

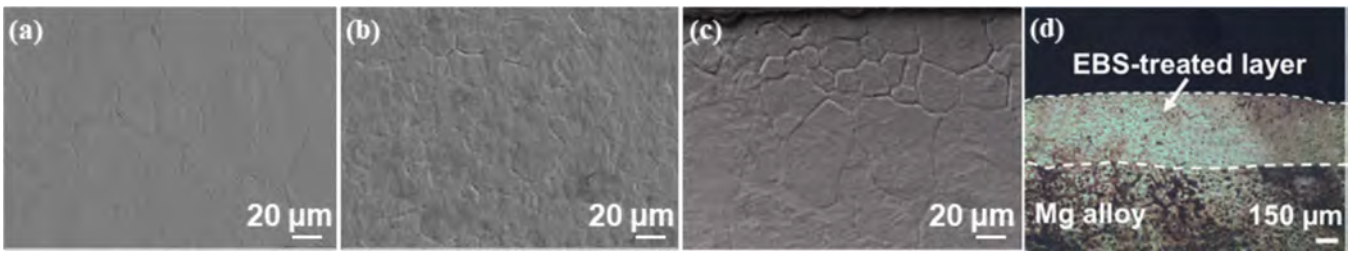

FIG. 1. (a) Surface microstructure of the M.P.-treated sample, (b) surface, and [(c) and (d)] Cross-sectional microstructure of EBS-treated samples.

Figure 2 exhibits the distribution of magnesium and aluminum elements in EBS-MAO-500. The Al concentration in the MAO coating increases, indicating that the reaction after EBS involves more Al atoms. In the near-surface of the Mg alloy, the Al concentration increases, but the content of magnesium decreases probably due to the heated vaporization of the Mg atom during EBS and the increase of Al-Mn compounds.[25] The larger Al concentration indicates that the solid solution of Al increases. It may provide a second layer against corrosion.[29] In summary, EBS produces refined Mg grains and larger Al concentration in the modified layer.

Figure 3 shows the XRD patterns of the M.P.-treated, EBS-treated, MAO-500, and EBS-MAO 500 samples. Mg is the primary constituent. There is only a small amount of Al_8Mn_5 in the M.P.-treated and EBS-treated samples, whereas MgO and Mg_2SiO_4 are the main ingredients with trace Mg_2SiO_3 in both coatings. No diffraction peak of MgF_2 is observed, possibly due to its amorphous structure and low content.

Figure 4 depicts the cross-sectional micrographs of the EBS-MAO and MAO coatings. The EBS-MAO and MAO coatings contain an inner barrier layer and a lateral microporous layer. Gases produced in the MAO process led to the micro-pores in the coating and thermal stress that existed in rapidly solidified molten oxide caused the formation of microcracks. The EBS-MAO coating interface became smoother, more homogeneous, and denser with fewer microcracks and micro-pores. Smaller surface roughness provides more and smaller discharge channels during MAO and smaller discharge channels frequently result in denser coatings.[18] The difference in the cross-sectional microstructure between the EBS-MAO and MAO coatings stems from grain refinement in the substrate by EBS.

The mean thickness of the EBS-MAO and MAO coatings is shown in Fig. 5 and the thickness of both layers increases with the discharge voltage. The EBS-MAO coatings are slightly thicker (1%–8.5%). According to the growth characteristics of MAO coatings, a grain-refined surface leads to the formation of uniform and nondestructive micro-discharges. On the other hand, the grain-refined surface provides more locations for plasma discharges in the initial surface passivation film.[18] These two reasons explain the larger

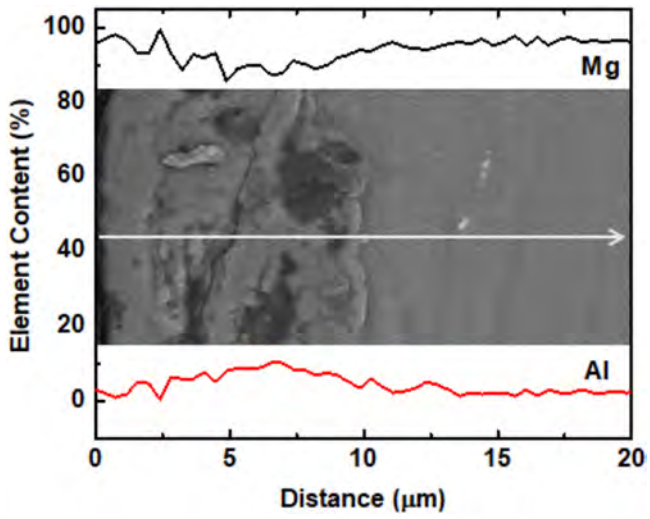

FIG. 2. Distribution of magnesium and aluminum elements in sample EBS-MAO-500.

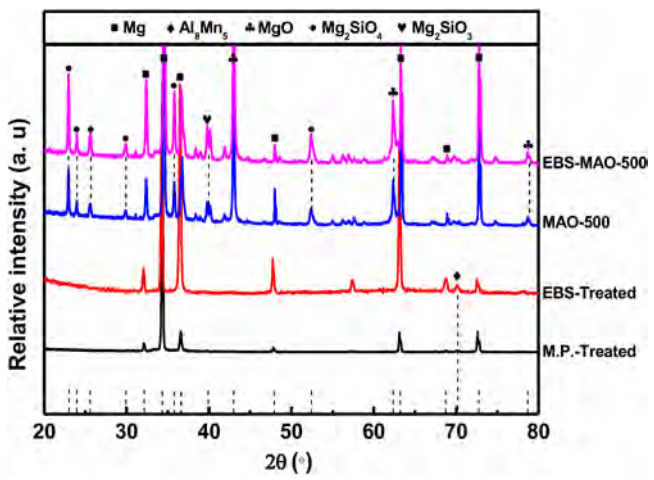

FIG. 3. XRD patterns of the samples M.P.-treated, EBS-treated, MAO-500 and EBS-MAO-500.

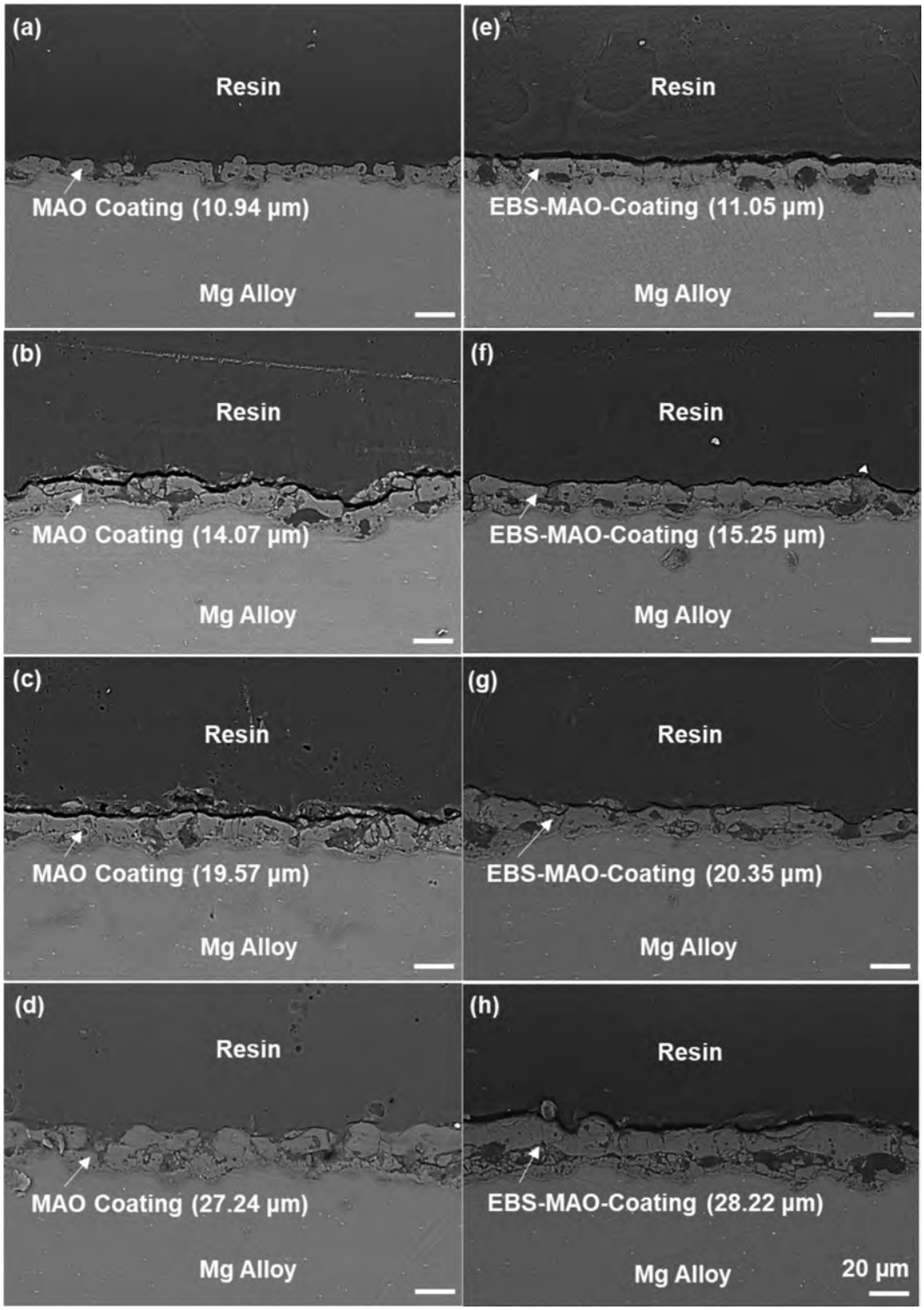

FIG. 4. Cross-sectional micrographs of MAO series: (a) MAO-460, (b) MAO-480, (c) MAO-500, (d) MAO-520 and EBS-MAO series: (e) EBS-MAO-460, (f) EBS-MAO-480, (g) EBS-MAO-500, (h) EBS-MAO-520.

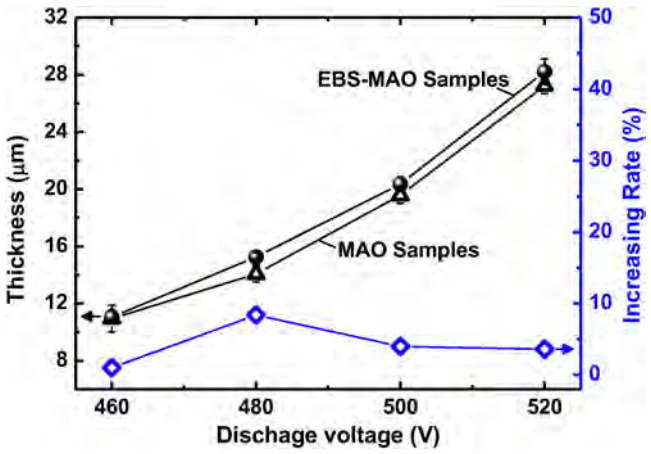

FIG. 5. Coating thickness of MAO and EBS-MAO series and the increasing rate in thickness between them.

coating thickness of the EBS-MAO samples. Table II shows that the presence of O, F, Mg, Al, Si, and EBS does not alter the composition. The Si concentration increases, implying that more electrolyte is involved in MAO after EBS. EBS produces many crystal defects and the nonequilibrium structure of the strengthened layer accelerates the chemical reactions in MAO.[30,31]

To investigate the effects of EBS on MAO, the discharge characteristics are determined. The curve of the current density (discharge current divided by surface area) versus time during MAO is depicted in Fig. 6. There are two distinctive regions, namely, the large gradient and small gradient sections. The large gradient section represents the original passivation layer growth and the current density increases steeply. After a coating with several micrometers of thickness is produced, the coating experiences a dielectric breakdown. The location with low coating resistance is easy to break down. Therefore, the MAO process includes the interaction of high temperature, melting, and solidification. The small gradient section reflects the forming process of the coating.

Compared to the M.P.-treated Mg alloy, the peak current density in the MAO process of the EBS-treated one is larger. The current density is related to the electrolyte and metal resistance when the discharge voltage is maintained at a certain value.[32] Since the conductivity of the electrolyte is the same for the same composition, the difference in the peak current density is affected dominantly by the substrate conditions, that is, the crystalline size. Oxygen is produced from the aqueous solution during MAO and it gathers around the metal. An intense electric field ionizes oxygen to produce plasma.[33] As reported previously,[33,34] oxygen diffuses and congregates easily at grain boundaries. Thus, breakdown occurs in the location with an intense electric field. Based on the above, breakdown may also occur at grain boundaries in the Mg alloy where oxygen is abundant. As for the EBS-treated samples, the refined grains raise the breakdown area and so the peak current density in MAO is larger. It also takes a longer time to reach the peak current and it may also be due to the refined grains. The grain boundaries scatter electrons under polarization conditions to impede the flow of electrons.[35] It is, thus, reasonable that the EBS-MAO sample exhibits a late appearance of the peak current density.

TABLE II. Composition of the ceramic layers in MAO and EBS-MAO series.

	Elements (at. %)				
Samples	O	F	Mg	Al	Si
MAO-460	54.3	1.9	32.1	0.7	11.0
MAO-480	53.4	2.3	32.4	0.8	11.1
MAO-500	53.6	2.0	31.9	0.7	11.8
MAO-520	55.0	2.5	30.2	0.8	11.5
EBS-MAO-460	54.2	1.4	32.9	0.7	10.8
EBS-MAO-480	50.9	1.7	33.8	1.1	12.5
EBS-MAO-500	52.3	1.6	33.0	0.8	12.3
EBS-MAO-520	53.3	2.4	30.3	0.6	13.4

The tendency of the current density change is related to the plasma behavior during oxide growth by considering the constructive and destructive nature of the plasma discharge. The current density is lower in the later stage of MAO of the EBS-treated Mg alloy, especially at a high positive voltage, implying that the coating thickness is greater or compactness is larger than that of the M.P.-treated samples.[36] Figure 7 depicts the micro-pores configuration of the EBS-MAO and MAO coatings processed by IMAGEJ software. The MAO coating has the typical microporous structure and the micro-pores are round or oval. Figure 8(a) shows the porosity of the micro-pores of different sizes. The porosity of the EBS-MAO coatings is lower, especially at large discharge voltages. Although the porosity decreases with discharge voltages, the porosity of the EBS-MAO coatings decreases at a faster rate. It decreases by 47.8% at a positive discharge voltage of 520 V and the reduced porosity may enhance the corrosion resistance.

Figure 8(b) shows the ratio of pores in a certain size range in all pores (ratio of pores). At the beginning of the MAO process, tiny discharge channels are formed and so the ratio of micro-pores with a size of 0–1 μm exceeds 50% in the EBS-MAO and MAO coatings subjected to different discharge voltages. As the layers are formed, the small micro-pores are relatively easy to break down to create larger micro-pores. The proportion of micro-pores larger than 2 μm in EBS-MAO-520 is significantly smaller than that of MAO-520. As shown in Fig. 6, the discharge voltage and current density are nearly constant. Therefore, the energy density of EBS-MAO is smaller in comparison with MAO alone due to more grain boundaries providing more reaction sites. And some earlier papers[37,38] suggest that the energy in a unit area determines the size of pores. Consequently, smaller micro-discharge channels are formed in the subsequent spark discharge stage.[18] In addition, the lower surface roughness after EBS weakens the local discharge, resulting in a more uniform distribution and smaller micro-pores.[39–41] As a result, there are fewer large pores in the EBS-MAO coatings than in the MAO coatings.

The influence of EBS on the surface and cross-sectional microstructure of the MAO coating is described as follows. First, EBS reduces the roughness of the substrate surface and it is easier

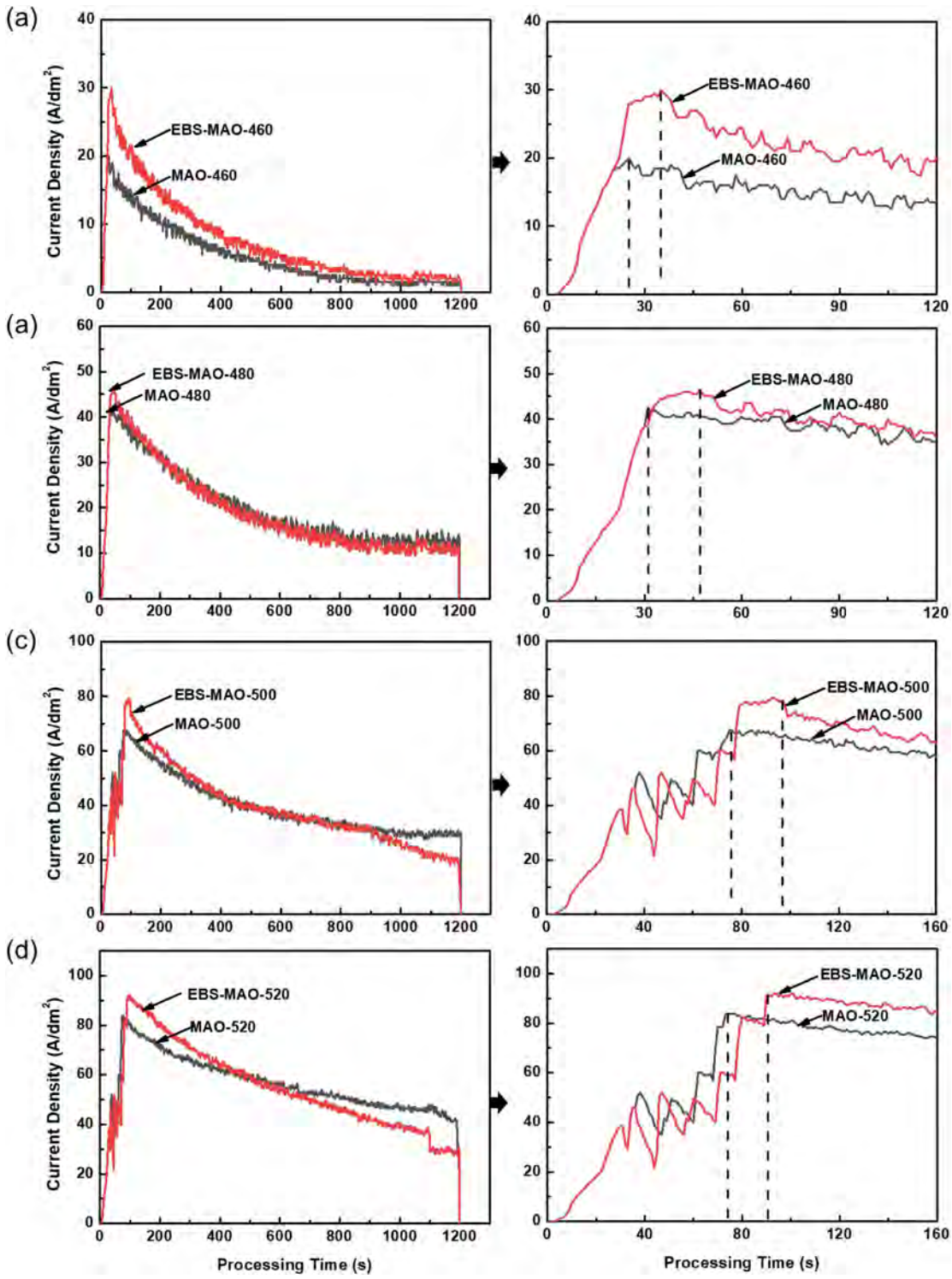

FIG. 6. Current density vs. time curves of (a) EBS-MAO-460/MAO-460, (b) EBS-MAO-480/MAO-480, (c) EBS-MAO-500/MAO-500, and (d) EBS-MAO-520/MAO-520 with corresponding local amplification.

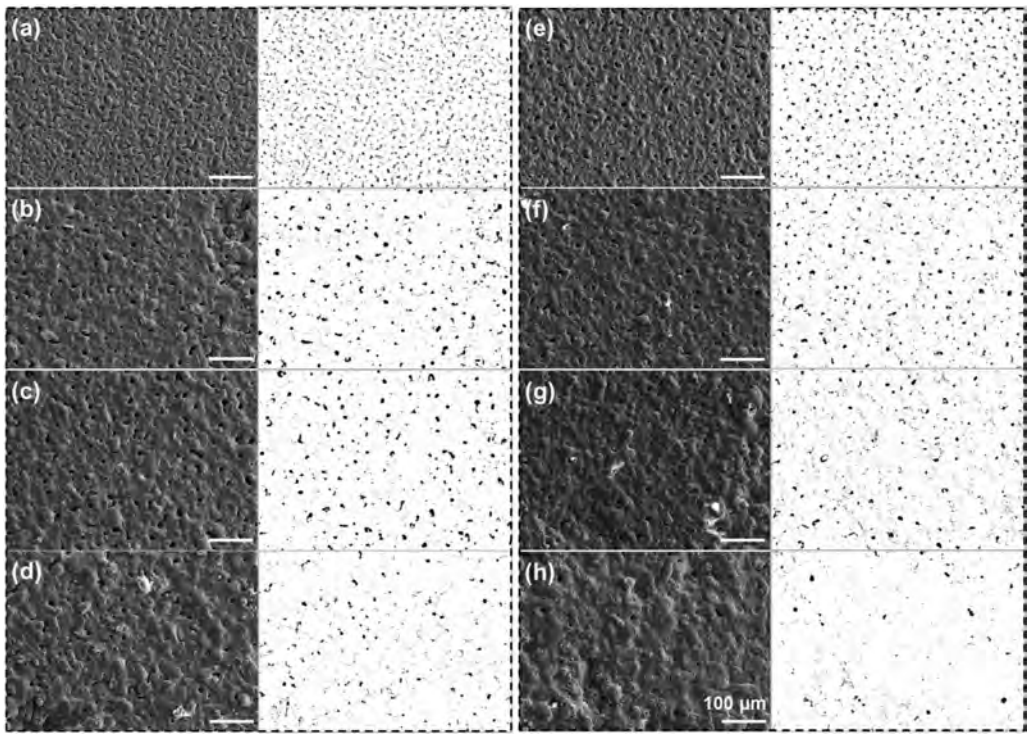

FIG. 7. Surface micrographs with the corresponding images by IMAGEJ of MAO series: (a) MAO-460, (b) MAO-480, (c) MAO-500, (d) MAO-520, and EBS-MAO series: (e) EBS-MAO-460, (f) EBS-MAO-480, (g) EBS-MAO-500, (h) EBS-MAO-520.

to obtain uniformly distributed micro-pores and a smooth interface between the Mg alloy and coatings. Second, after EBS, the grains in the Mg alloy are refined rendering them to be conducive to the micro-discharge. The improved micro-discharge promotes the growth of uniform and nondestructive coatings in MAO, reduces porosity, and improves the coating microstructure.

B. Electrochemical behaviors

1. Potentiodynamic polarization measurements

Figure 9(a) displays the potentiodynamic polarization curves of the M.P.-treated, EBS-treated, MAO-520, and EBS-MAO-520 samples. Compared to the M.P.-treated sample, the curve of the EBS-treated sample shifts to higher potentials and smaller current densities. Therefore, the corrosion performance of the M.P.-treated sample improves due to lower roughness and finer grain size after EBS.[42] Figure 9(a) also shows that the curves of MAO-520 and EBS-MAO-520 shift to higher potentials and i_{corr} of all the MAO coatings is almost 10 times lower than that of the Mg alloy, regardless of whether they undergo EBS or not as shown in Table III, which indicates that the MAO coatings play an excellent protective role. Table III also shows that the corrosion performance of the EBS-MAO samples is higher than that of the MAO samples, especially at high positive voltages. E_{corr} and i_{corr} of MAO-520 are -1.460 V and 2.012×10^{-6} A/cm^2, whereas those of EBS-MAO-520 are -1.162 V and 6.423×10^{-7} A/cm^2, respectively. i_{corr} decreases by almost 1/3. The micro-pores in the coating provide passages for corrosive ions to reach the Mg alloy substrate. A high porosity together with a small coating thickness is the reason for the low corrosion performance of the MAO samples. Besides, the compact and thick coating of EBS-MAO delivers a better anticorrosion performance. As mentioned above, the EBS-MAO samples are thicker and the denser microstructure increases the corrosion resistance.

2. EIS measurements

Figure 9(b) shows the Nyquist plots of the M.P.-treated, EBS-treated, MAO, and EBS-MAO samples. The diameter (capacitive loops) of the EBS-MAO samples is larger, especially at higher discharge voltages, demonstrating that the EBS-MAO coatings enhance the corrosion performance.[43] Figure 9(c) displays the ECM. The evolution of the coating system and the corrosion processes were quantified by fitting the impedance spectra using appropriate ECM. The applicability of the model has been verified by comparing chi-square values which have typical parameters of around 0.5×10^{-3} indicating a good fitting. Table III shows values in the circuit. R_s involved represents the resistance between the Mg alloy and reference electrodes. The contact resistance of the passivation film and solution is R_1, and charge-transfer resistance with the substrate is R_2. As for the MAO and EBS-MAO samples, they

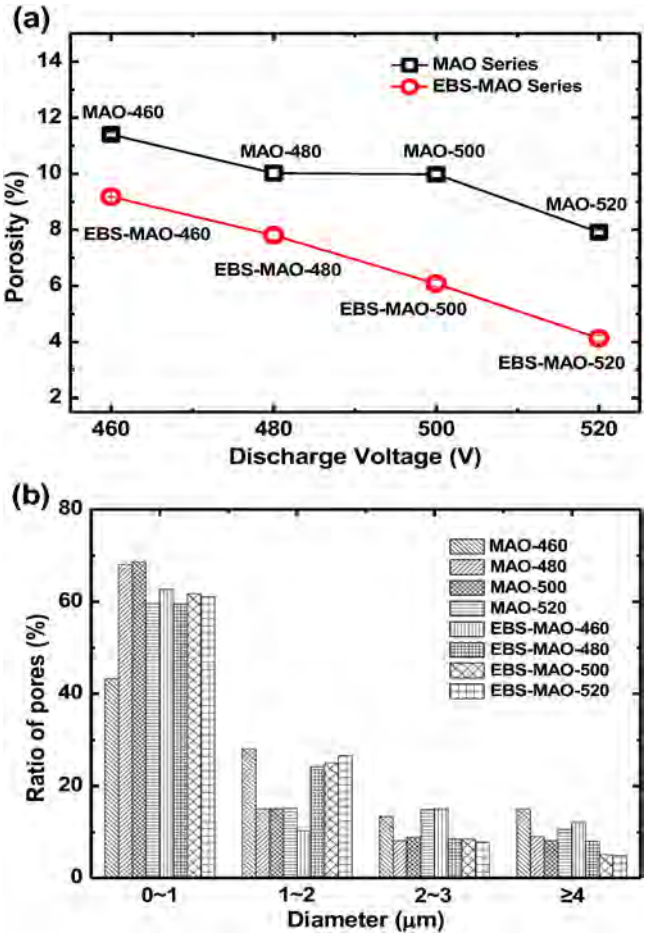

FIG. 8. (a) Porosity and (b) ratio of pores of the MAO and EBS-MAO series.

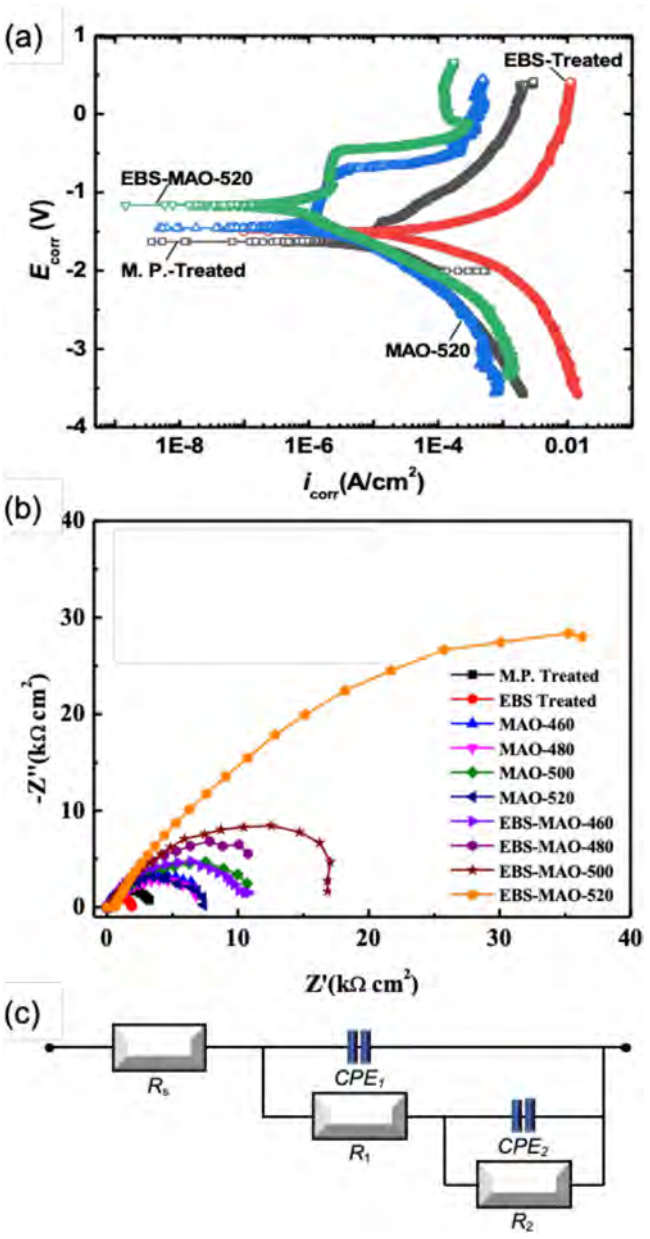

FIG. 9. (a) Potentiodynamic polarization curves of the samples: M.P.-treated, EBS-treated, MAO-520 and EBS-MAO-520, and (b) EIS Nyquist plots of the samples: M.P.-treated, EBS-treated, MAO and EBS-MAO series. (c) Equivalent circuit model used for fitting the EIS results of MAO and EBS-MAO series.

donate the resistance of the inner and outer layers, respectively. *CPE-Y_1* and *CPE-Y_2* represent the dielectric behavior of the inner and outer layers, respectively.[16]

During MAO, at low voltages of 460 and 480 V (EBS-MAO-460 and EBS-MAO-480), R_1 or R_2 increases slightly indicating a minor positive influence of EBS on the corrosion performance of the MAO coatings consistent with the polarization curve and smooth surface morphology. However, at larger voltages of 500 V (EBS-MAO-500), and especially 520 V (EBS-MAO-520), R_2 increases substantially from 2.22×10^4 to $1.14 \times 10^5\ \Omega\,cm^2$. R_2 of the EBS-MAO sample is ten times bigger than that of the MAO sample. Furthermore, *CPE-Y_2* of the EBS-MAO-520 ($5.99 \times 10^{-8}\ \Omega^{-1}\,s^n\,cm^{-2}$) is ten times smaller than that of the MAO sample ($4.44 \times 10^{-7}\ \Omega^{-1}\,s^n\,cm^{-2}$), indicating the least exposed surface area and porosity. Therefore, the absorbability of dielectric charges would be least, which would obstruct charge transfer and corrosive dissolution of metal ions.[44] The dense layer is the reaction product of metal ions and electrolyte anions in the initial micro-arc oxidation stage and growth depends on the substrate conditions. EBS improves the roughness and microstructure of the Mg alloy and so denser and more uniform layers are formed. At the same time, owing to the nondestructive and uniform microdischarge, the outer porous layer with high resistance turns into a uniform and dense layer.

TABLE III. Potentiodynamic polarization and EIS Nyquist analysis of the M.P.-treated, EBS-treated, MAO, and EBS-MAO samples.

				CPE_1			CPE_2		
Samples	E_{corr} (V)	i_{corr} (A cm^{-2})	R_s (Ω cm^2)	Y_1	n_1	R_1 (Ω cm^2)	Y_2	n_2	R_2 (Ω cm^2)
M. P.-Treated	−1.672	1.671×10^{-5}	33.15	1.33×10^{-6}	0.93	4.2×10^{2}	1.25×10^{-6}	0.91	1.64×10^{3}
EBS-Treated	−1.521	1.144×10^{-5}	39.56	8.77×10^{-6}	0.95	6.4×10^{2}	4.99×10^{-7}	0.93	1.69×10^{3}
MAO-460	−1.493	8.560×10^{-6}	45.5	3.84×10^{-7}	0.76	1.40×10^{3}	2.62×10^{-7}	0.98	1.93×10^{4}
MAO-480	−1.471	2.732×10^{-6}	40.6	3.65×10^{-7}	0.88	1.42×10^{3}	1.98×10^{-7}	0.84	1.85×10^{4}
MAO-500	−1.565	2.990×10^{-6}	44.2	6.18×10^{-7}	0.88	1.55×10^{3}	4.90×10^{-7}	0.90	1.10×10^{4}
MAO-520	−1.460	2.012×10^{-6}	48.3	1.38×10^{-7}	0.72	2.60×10^{3}	4.44×10^{-7}	0.84	2.22×10^{4}
EBS-MAO-460	−1.534	6.301×10^{-6}	30.84	1.57×10^{-6}	0.58	2.52×10^{3}	2.92×10^{-7}	0.75	1.58×10^{4}
EBS-MAO-480	−1.454	1.560×10^{-6}	32.54	1.69×10^{-7}	0.69	1.33×10^{3}	3.65×10^{-7}	0.92	1.89×10^{4}
EBS-MAO-500	−1.532	9.267×10^{-7}	33.28	1.31×10^{-6}	0.83	2.95×10^{3}	6.08×10^{-8}	0.88	5.02×10^{4}
EBS-MAO-520	−1.162	6.423×10^{-7}	35.26	3.24×10^{-7}	0.78	6.08×10^{3}	5.99×10^{-8}	0.69	1.14×10^{5}

3. Immersion tests

Figure 10(a) depicts the microscopic images of the MAO and EBS-MAO specimens for different immersion durations. Noticeable corrosion pits appear from the surface of MAO-460/520 and EBS-MAO-460 samples after immersion for 60 h. As immersion proceeds, the corrosion pits become bigger and after immersion for 220 h, the surface exhibits severe localized corrosion. However, no corrosion craters are visible until 492 h, indicating that the corrosion performance of EBS-MAO-520 behaves better during different immersion durations.

During the immersion tests, the pH of the solution is measured and Fig. 10(b) shows the pH changes of MAO-460/520 and EBS-MAO-460/520 during 20 days of immersion. The curve is more or less composed of three stages. In the first stage (I), the *p*H of all the samples increases. The chemical reaction involved is as follows: $MgO + H_2O \rightarrow Mg(OH)_2$. In the second stage (II), which is also the stage when the corrosion starts to contact the Mg alloy, it shows an accelerated increase in the *p*H due to more alkaline ions. The reactions involved are as follows: (1) (anode) $Mg \rightarrow Mg^{2+} + 2e^-$; (2) (cathode) $2H_2O + 2e^- \rightarrow H_2 + 2OH^-$ In the third stage (III), the increase rate of *p*H decreases. A large number of magnesium ions and chloride ions in the pitting may react as follows: $2Mg^{2+} + 6H_2O + Cl^- \rightarrow 3H^+ + Mg_2(OH)_3Cl{\cdot}3H_2O$. Therefore, the increase in H^+ concentration leads to a decreasing rate. However, the *p*H of EBS-MAO-460/520 has a slowly increasing trend. The reasons could be closely related to the low reaction degree resulting from low porosity, refined Mg grains, uniform distribution of the Al-Mn phase, and larger Al concentration in the modified layer.

4. Corroded cross-sectional morphology

To better understand how EBS affects the corrosion behavior of the MAO coatings, the corroded cross-sectional images are examined by SEM. Figures 11(a) and 11(b) show that the corroded depth of MAO-460/520 is up to 1000 μm. Obviously, the coating fails to protect the underlying Mg alloy because the corrosion medium can penetrate deeply and corrode the substrate [Figs. 11(e) and 11(f)]. In contrast, the corrosion area in EBS-MAO-460/520 is smaller [Figs. 11(c) and 11(d)]. As shown in Figs. 11(g) and 11(h),

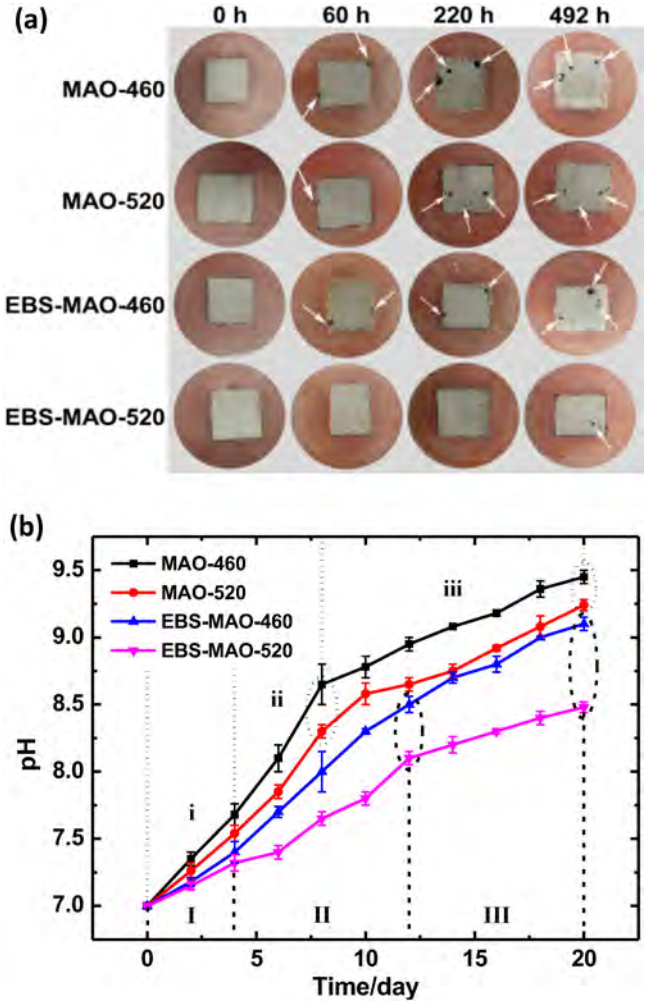

FIG. 10. (a) Photographs and (b) *p*H changes of samples: MAO-460, MAO-520 and EBS-MAO-460, EBS-MAO-520 after immersion in 3.5 wt. % NaCl solution for a different time.

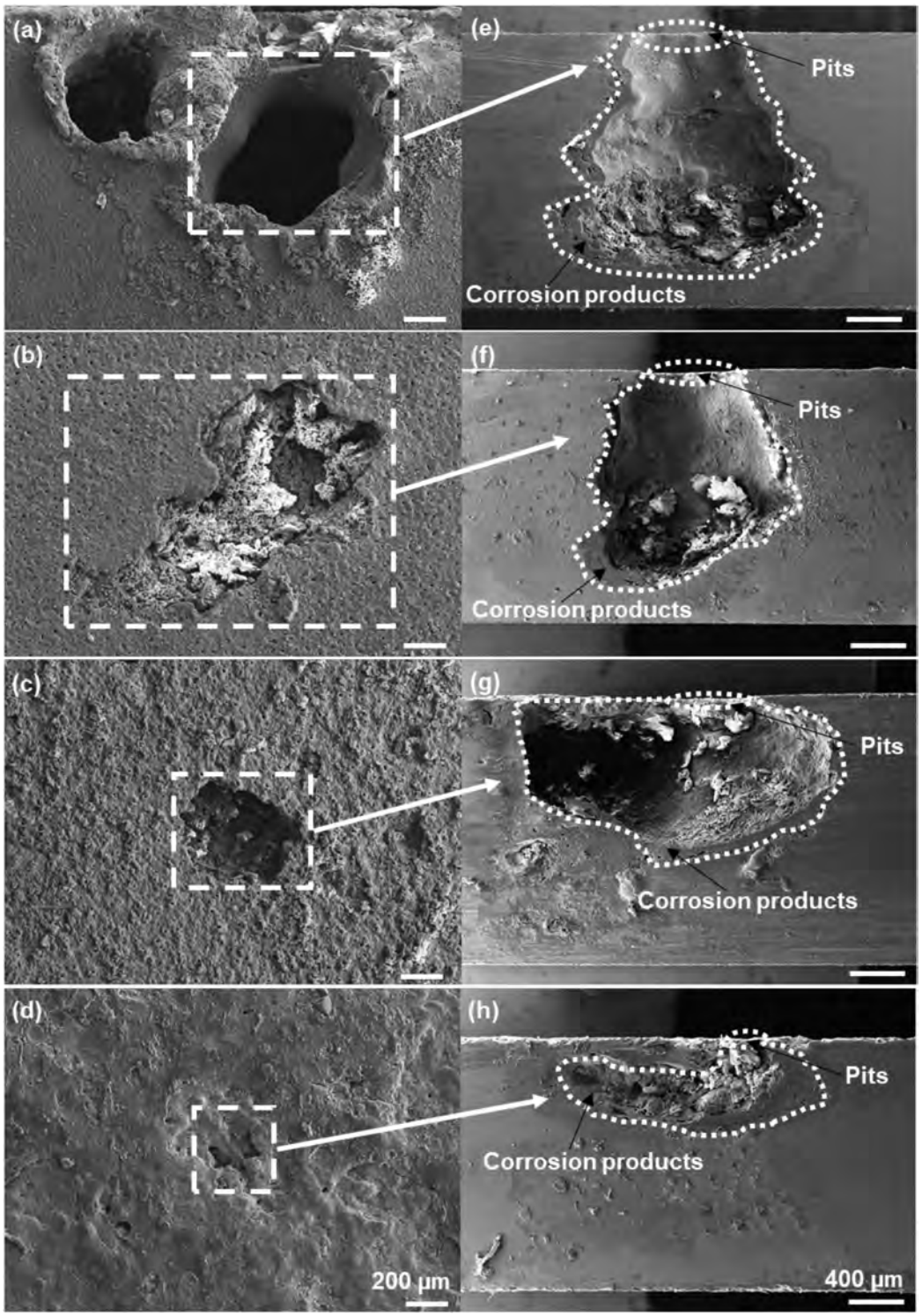

FIG. 11. Surface and cross-sectional micrographs of samples: [(a) and (e)] MAO-460, [(b) and (f)] MAO-520, [(c) and (g)] EBS-MAO-460, and [(d) and (h)] EBS-MAO-520 after immersion in the 3.5 wt. % NaCl solution for 492 h.

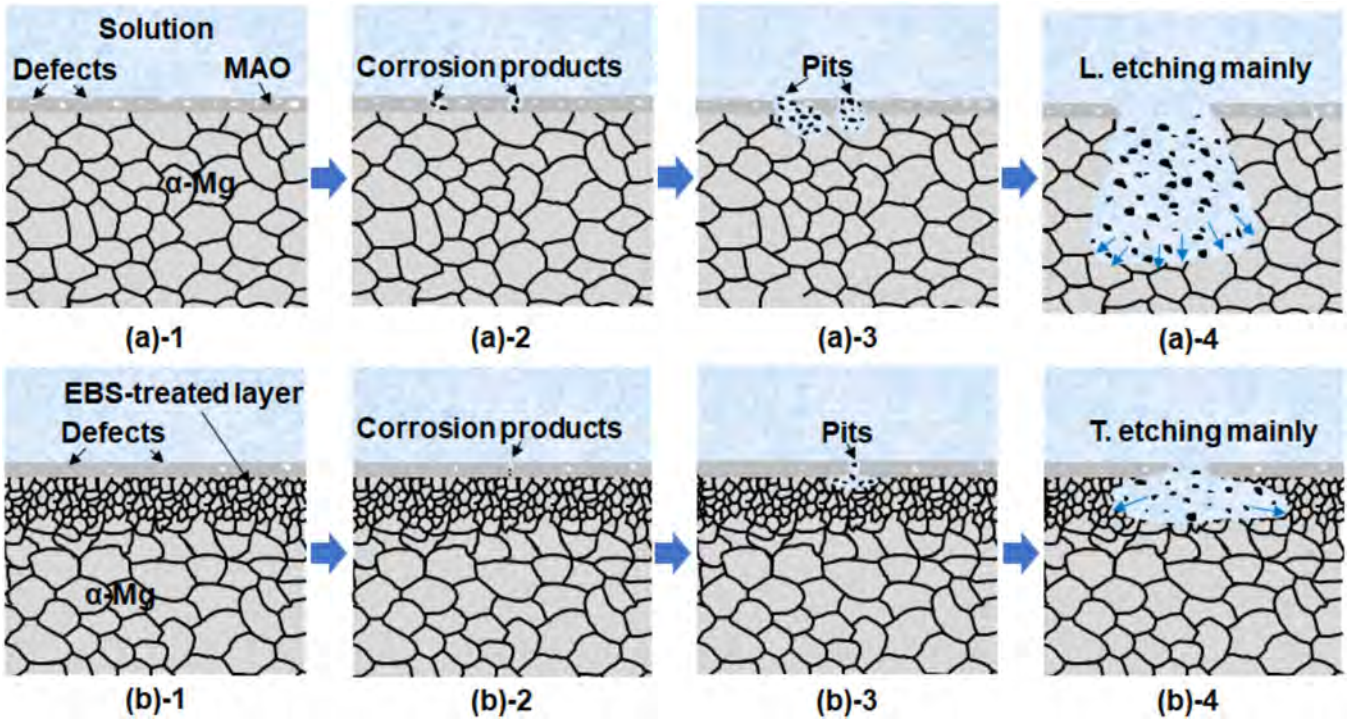

FIG. 12. Schematic diagram illustrating the corrosion process of (a) MAO coating and (b) EBS-MAO coating.

the craters tend to expand horizontally (transverse etching—T. etching), indicating that EBS enhances the longitudinal corrosion resistance. Longitudinal etching (L. etching) can reduce the load-bearing capacity of the sample and so it is essential to reduce erosion in the longitudinal direction.

5. Corrosion mechanism

Based on the experimental results, Fig. 12 presents the schematic of the corrosion behavior of MAO and EBS-MAO samples at the beginning as well as during early, intermediate, and long-term immersion. Micro-pores and micro-cracks frequently exist in the MAO coatings, which increase the chance of the corrosive medium to reach the substrate to cause fast corrosion like the MAO-coated Mg alloy [Fig. 12(a)-1]. The formation of corrosion products (mainly $Mg(OH)_2$) accumulates at the interface during different immersion durations [Figs. 12(a)-2–12(a)-3]. The stress that originated from the increasing volume of corrosion products even brings about local delamination.[45,46] Therefore, the coating fails to protect the Mg alloy from severe localized corrosion [Fig. 12(a)-4]. However, EBS reduces the number of large pores and produces a denser coating to impede penetration of the corrosive medium [Fig. 12(b)-1]. Consequently, fewer corrosion products are produced [Figs. 12(b)-2 and 12(b)-3]. The MAO coating decelerates corrosion, thus resulting in less stress and longer protection of the substrate.

The AZ31 Mg alloy is composed of α-Mg with Al_8Mn_5, the latter has higher E_{corr}[47] and generally quickens decomposition of the former. Pitting preferentially germinates in the coarse-grained area. On the other hand, micro-galvanic corrosion is improved due to the refinement of α-Mg grains and the uniform distribution of the Al_8Mn_5 phase. In addition, enrichment of Al in the EBS-treated samples decreases the dissolution of the α-Mg matrix result from the smaller E_{corr} difference between the α-Mg matrix and Al_8Mn_5 phase. These factors lead to the morphology shown in Figs. 11(g) and 11(h). The SEM images of the corroded surfaces imply that the EBS-treated layer is a barrier against the longitudinal expansion of corrosion [Fig. 12(b)-4].

IV. SUMMARY AND CONCLUSIONS

EBS pretreatment and deposition of compact ceramic coatings by the MAO process improve the properties of the Mg alloy. EBS reduces the surface roughness, refines the magnesium grains, and enriches the Al content. The improved corrosion resistance arises from smaller roughness and crystalline size. During MAO, the EBS-treated samples show larger peak current densities and it takes a longer time to initiate micro-discharges at different discharge voltages due to grain refinement. The improved discharge characteristics in MAO after EBS reduce the porosity of the MAO coatings and increase the compactness of the microstructure, especially at bigger positive voltages. Thus, better corrosion protection is achieved by performing EBS and MAO compared to MAO alone.

The compact coating and refined grains are responsible for the improved anticorrosion behavior.

ACKNOWLEDGMENTS

The work was supported by the National Natural Science Foundation of China (No. 51975530), Department of Education of Zhejiang Province (No. Y202249101), Heilongjiang Natural Science Foundation (No. LH2022E102), the City University of Hong Kong Strategic Research Grant (SRG No. 7005505), and the City University of Hong Kong Donation Research Grant (No. DON-RMG 9229021).

AUTHOR DECLARATIONS

Conflict of Interest

The authors have no conflicts to disclose.

Author Contributions

Yinghe Ma: Conceptualization (equal); Funding acquisition (equal); Investigation (equal); Methodology (equal); Project administration (equal); Writing – original draft (equal). **Jinhui Mei:** Data curation (equal); Investigation (equal); Resources (equal). **Junxin Ouyang:** Data curation (equal); Investigation (equal); Resources (equal). **Peng Wu:** Data curation (equal); Resources (equal). **Sai Wang:** Writing – review & editing (equal). **Jianguo Yang:** Funding acquisition (equal); Supervision (equal); Writing – review & editing (equal). **Yanming He:** Writing – review & editing (equal). **Wenjian Zheng:** Visualization (equal); Writing – review & editing (equal). **Huaxin Li:** Visualization (equal); Writing – review & editing (equal). **Chuanyang Lu:** Writing – review & editing (equal). **Sendong Ren:** Writing – review & editing (equal). **Jianping Xu:** Funding acquisition (equal); Writing – review & editing (equal). **Paul K. Chu:** Funding acquisition (equal); Supervision (equal); Writing – review & editing (equal).

DATA AVAILABILITY

The data that support the findings of this study are available from the corresponding authors upon reasonable request.

REFERENCES

[1]C. Zhang, C. Liu, X. Li, K. L. Liu, G. Y. Tian, and J. S. Wang, Corros. Sci. **195**, 110010 (2022).
[2]U. Rokkala, A. Jana, S. Bontha, M. R. Ramesh, and V. K. Balla, Surf. Coat. Technol. **425**, 127708 (2021).
[3]J. Wang, T. Li, H. X. Li, Y. Z. Ma, K. N. Zhao, C. L. Yang, and J. S. Zhang, J. Magnesium Alloys **9**, 1632 (2021).
[4]M. Esmaily, J. E. Svensson, S. Fajardo, N. Birbilis, G. S. Frankel, S. Virtanen, R. Arrabal, S. Thomas, and L. G. Johansson, Prog. Mater. Sci. **89**, 92 (2017).
[5]T. W. Clyne and S. C. Troughton, Int. Mater. Rev. **64**, 127 (2019).
[6]R. Arrabal, A. Pardo, M. C. Merino, M. Mohedano, P. Casajús, E. Matykina, P. Skeldon, and G. E. Thompson, Corros. Sci. **52**, 3738 (2010).
[7]K. Liu, M. Zheng, Y. Liu, J. Yang, and Y. Yao, IEEE Trans. Ind. Inform. **19**, 6429 (2023).
[8]K. Liu, Q. Yu, Y. Liu, J. Yang, and Y. Yao, IEEE Trans. Instrum. Meas. **71**, 4506411 (2022).
[9]K. Liu, K. Huang, S. Sfarra, J. Yang, L. Yi, and Y. Yuan, Quant. Infr. Therm. J. **20**, 25 (2023).
[10]J. S. Cai, F. H. Cao, L. R. Chang, J. J. Zheng, J. Q. Zhang, and C. N. Cao, Appl. Surf. Sci. **257**, 3804 (2011).
[11]Y. Mori, A. Koshi, J. S. Liao, H. Asoh, and S. Ono, Corros. Sci. **88**, 254 (2014).
[12]J. J. Zhuang, Y. Q. Guo, N. Xiang, Y. M. Xiong, Q. S. Hu, and R. G. Song, Appl. Surf. Sci. **357**, 1463 (2015).
[13]M. Kaseem, S. Fatimah, N. Nashrah, and Y. G. Ko, Prog. Mater. Sci. **117**, 100735 (2021).
[14]M. Kaseem and Y. G. Ko, Mater. Lett. **221**, 196 (2018).
[15]M. Kaseem, T. Hussain, S. H. Baek, and Y. G. Ko, Mater. Des. **193**, 108823 (2020).
[16]M. Kaseem, T. Hussain, U. R. Zeeshan, H. W. Yang, B. Dikici, and Y. G. Ko, Chem. Eng. J. **420**, 129737 (2021).
[17]M. Kaseem, B. Dikici, A. Dafali, and A. Fattah-alhosseini, J. Magnesium Alloys **11**, 1618 (2023).
[18]S. Fatimah, H. W. Yang, M. P. Kamil, and Y. G. Ko, Appl. Surf. Sci. **477**, 60 (2019).
[19]X. Yang, B. Wang, W. P. Gu, Z. Y. Zhang, Y. Q. Chen, T. Wu, Q. B. Wang, and H. P. Tang, Surf. Coat. Technol. **428**, 127880 (2021).
[20]Y. H. Gu, L. L. Chen, W. Yue, P. Chen, F. Chen, and C. Y. Ning, J. Alloy. Compd. **664**, 770 (2016).
[21]S. Z. Hao, Y. Qin, X. X. Mei, B. Gao, J. X. Zuo, Q. F. Guan, C. Dong, and Q. Y. Zhang, Surf. Coat. Technol. **201**, 8588 (2007).
[22]J. E. Gray and B. J. Luan, J. Alloy. Compd. **336**, 88 (2002).
[23]C. Taltavull, B. Torres, A. J. Lopez, P. Rodrigo, E. Otero, A. Atrens, and J. Rams, Mater. Des. **57**, 40 (2014).
[24]G. Abbas, Z. Liu, and P. Skeldon, Appl. Surf. Sci. **247**, 347 (2005).
[25]C. C. Liu, J. Liang, J. S. Zhou, Q. B. Li, and L. Q. Wang, Appl. Surf. Sci. **382**, 47 (2016).
[26]F. Iranshahi, M. B, F. Nasiri, G. Warchomicka, and C. Sommitsch, J. Magnesium Alloys **10**, 707 (2022).
[27]F. Morini, M. Bestetti, S. Franz, A. Vicenzo, A. Markov, and E. Yakovlev, Surf. Coat. Technol. **420**, 127351 (2021).
[28]F. Iranshahi, M. B. Nasiri, F. G. Warchomicka, and C. Sommitsch, J. Magnesium Alloys **8**, 1314 (2020).
[29]G. L. Makar and J. Kruger, J. Electrochem. Soc. **137**, 414 (1990).
[30]Z. Q. Yao, Y. Ivanisenko, T. Diemant, A. Caron, A. Chuvilin, J. Z. Jiang, R. Z. Valiev, M. Qi, and H.-J. Fecht, Acta Biomater. **6**, 2816 (2010).
[31]N. Ao, D. X. Liu, X. H. Zhang, and C. S. Liu, Appl. Surf. Sci. **489**, 595 (2019).
[32]S. Ikonopisov, A. Girginov, and M. Machkova, Electrochim. Acta **24**, 451 (1979).
[33]A. L. Yerokhin, X. Nie, A. Leyland, A. Matthews, and S. J. Dowey, Surf. Coat. Technol. **122**, 73 (1999).
[34]X. Yin, Y. Wang, B. Liu, and X. B. Luo, Surf. Interface Anal. **44**, 276 (2012).
[35]A. F. Mayadas and M. Shatzkes, Phys. Rev. B **1**, 1382 (1970).
[36]A. L. Yerokhin, X. Nie, A. Leyland, and A. Matthews, Surf. Coat. Technol. **130**, 195 (2000).
[37]W. H. Song, Y. K. Jun, Y. Han, and S. H. Hong, Biomaterials **25**, 3341 (2004).
[38]D. Q. Wei, Y. Zhou, D. C. Jia, and Y. M. Wang, Mater. Chem. Phys. **104**, 177 (2007).
[39]H. Hanjun, C. Zhen, L. Xingguang, F. Xingguo, Z. Yugang, Z. Kaifeng, and Z. Hui, Surf. Coat. Technol. **349**, 593 (2018).
[40]B. Y. Yoo, K. R. Shin, D. Y. Hwang, D. H. Lee, and D. H. Shin, Appl. Surf. Sci. **256**, 6667 (2010).
[41]N. Nashrah, M. P. Kamil, D. K. Yoon, Y. G. Kim, and Y. G. Ko, Appl. Surf. Sci. **497**, 143772 (2019).
[42]L. F. Ye *et al.*, J. Mater. Res. Technol. **16**, 1673 (2022).
[43]A. Nishikata, Y. Ichihara, and T. Tsuru, Corros. Sci. **37**, 897 (1995).
[44]T. Hussain, M. Kaseem, and Y. G. Ko, Corros. Sci. **170**, 108663 (2020).
[45]J. Liang, P. B. Srinivasan, C. Blawert, M. Störmer, and W. Dietzel, Electrochim. Acta **54**, 3842 (2009).
[46]F. Muhaffel, F. Mert, H. Cimenoglu, D. Höche, M. L. Zheludkevich, and C. Blawert, Surf. Coat. Technol. **269**, 200 (2015).
[47]A. Boby, A. Srinivasan, U. T. Pillai, and C. B. Pai, Mater. Des. **88**, 871 (2015).